Assessing the stability of underground caves through iSUMM (innovative, straightforward, user-friendly, mechanically-based method)

Federica Angela Mevoli[1*], Nunzio Luciano Fazio[1†], Michele Perrotti[2†] and Piernicola Lollino[3†]

Abstract

A huge number of sinkhole events has been recorded in different Italian urban areas, with an occurrence frequency largely increasing in the last decades, sometimes even causing loss of human lives. The main reason for such catastrophic events is the presence of man-made underground cavities, excavated within soft rocks, several decades ago and then abandoned, at shallow depths. Here, the possibility of interaction with overlying buildings and infrastructures and the corresponding sinkhole hazard is relatively high. In such contexts, the low mechanical properties of the soft rock formations where the cavities have been excavated, like those formed of calcarenites, which outcrop in large areas of Southern Italy, and their high susceptibility to weathering processes, represent one of the most important predisposing factors for instability. Therefore, assessing the stability of underground cavities is crucial for land management and planning purposes. The mechanically-based stability charts developed by Perrotti et al. (Int J Geomech 18(7):04018071, 2018) have proved to be a valid tool for preliminary stability assessment and, although allow to identify an eventual proneness of the cave to instability, they do not provide quantitative assessment about the safety margin itself. In that regard, this study intends to present the most recent outcomes obtained in the development of the methodology and is aimed at promoting an enhanced way for their application, so that the charts can become an operative tool for preliminary sinkhole hazard assessment in similar regions in the world.

Keywords Underground cavities, Sinkholes, Stability charts, Safety factor, Large-scale investigation, Numerical modeling

Introduction

Sinkholes are failure processes that can affect man-made or natural underground cavities as a consequence of a change in the loading or boundary conditions (Castellanza et al. 2018). Since the early 1900s, the Italian territory has been broadly characterized by sinkhole phenomena. Almost 5000 failure events, affecting both anthropogenic and natural caves, occurred between 1960 and 2018 throughout the Italian territory, with a considerable increase of the recorded failure events involving anthropogenic caves in the last two decades (Nisio 2009, 2017, 2018). In particular, in the Apulian Region (south-eastern Italy), the majority of sinkholes has been developed in caves created by human activities, so that the total amount of sinkholes in anthropogenic caves reaches about the 63.6% of the total recorded events (Parise 2012). In the past centuries, numerous underground environments have been excavated in the very soft calcarenite rocks largely outcropping in the region

†Nunzio Luciano Fazio, Michele Perrotti and Piernicola Lollino have contributed equally to this work.

*Correspondence:
Federica Angela Mevoli
federica.mevoli@irpi.cnr.it
[1] CNR - IRPI, Via Giovanni Amendola 122i, 70126 Bari, Italy
[2] ISPRA, Via Vitaliano Brancati 48, 00144 Rome, Italy
[3] Department of Earth and Geoenvironmental Sciences, University of Bari "Aldo Moro", Via Orabona 4, 70125 Bari, Italy

for different purposes, like the extraction of building materials, places of worship, anthropic settlements, etc. Later on, these underground cavities have been abandoned and, in some cases, the trace of their existence has been lost with the passing of the time (Parise 2010, 2012; Perrotti et al. 2018; Castellanza et al. 2018). Therefore, the stability of these underground environments has been frequently disregarded despite a massive urbanization process, spreading out in recent decades, which has led to the construction of buildings and infrastructures above pre-existing cavities, thus posing potential risks to properties and human lives (Fiore and Parise 2013). In similar situations, the interaction between the cavity and the overlying structures, and the stability of the overall system, can be influenced by several factors, such as the position of the cavity with respect to the above building structure, the rock susceptibility to weathering phenomena generated by water infiltration from the ground surface, leakages from hydraulic pipes and/or sewer networks, and the geomechanical properties of the rock in which the cavity has been dug (Aydan et al. 2005; Parise and Lollino 2011; Lollino et al. 2013; Ciantia et al. 2015; Lollino et al. 2021; Guenzi et al. 2022). Sinkhole failures were registered not only in Apulian municipalities like Gallipoli, Canosa di Puglia, Barletta and Altamura but also in other cities (as, for example, Marsala in the region of Sicily) where soft rock formations of Calcarenite, characterized by high porosity, low mechanical strength and high susceptibility to water-induced weakening processes, outcrop (Parise and Vennari 2017; Perrotti et al. 2019; Vattano et al. 2013). Although failure frequently occurs according to a brittle and rapid mechanism, the process that leads to instability can evolve within years or decades from the time of the excavation, as a consequence of slow mechanical degradation of the rock materials (Parise and Lollino 2011; Parise and Vennari 2017; Pellicani et al. 2017).

Nowadays, in order to investigate the cave stability from a quantitative point of view, it is possible to rely on several advanced technologies, each characterized by different level of reliability and accuracy. In preliminary investigations aiming at the stability assessment over a large number of cavities, analytical and phenomenological approaches are usually used in order to identify those cases at major risk (Gesualdo et al. 2001; Fraldi and Guarracino 2009; Carter 2014). Later on, more specific methods can be applied at the single cavity scale, as the early-warning systems that allows to monitor the microseismic noise emitted during the rock degradation and failure propagation (Evangelista et al. 1991; Contrucci et al. 2011), or it is even possible to adopt more sophisticated approaches like those based on the numerical modeling, which can address very complex stability problems in a reliable and efficient manner (Goodings and Abdulla 2002; Ferrero et al. 2010; Parise and Lollino 2011; Lollino et al. 2013; Fazio et al. 2017; Mancini et al. 2017; Castellanza et al. 2018). Although the latter are adequate at the single-cavity scale investigation, on the other hand the level of expertise and time required for their application might result in huge economical investments when dealing with a large number of cavities. For this reason, physically or mechanically based stability charts can be useful for offering an initial evaluation of an underground system stability, depending on its geometric and mechanical parameters (Federico and Screpanti 2003; Suchowerska et al. 2012). Many authors have contributed in developing stability charts to address different possible applications: for the case of spherical voids under axisymmetric conditions using the upper and lower bound finite element limit analysis (Keawsawasvong and Shiau 2022), for the roof stability evaluation of natural cavities in jointed rock masses when the failure mechanism is contained within the rock overburden thickness and does not intercept the ground level (Zhang et al. 2019), for the specific case of residual soils, allowing the investigation of the inverted strength profile usually observed in karst terrains (Drumm et al. 2009), to mention a few. Specifically, Perrotti et al. (2018) developed Finite Element Method (FEM)-based stability charts for underground man-made cavities in calcarenite rocks, as those largely diffused in the Southern Italy. These charts need really basic information about the geometry of the cavity cross-section, the information on the stress state of the rock mass and the rock mass geomechanical parameters. In particular, these graphs show four curves, representing cave failure conditions, so that a representative point of the investigated section that is above the failure curve indicates stable conditions, whereas a point below or along it represents an unstable condition. Although these mechanically-based stability charts are able to assess whether the section of a cavity is stable or not, they do not provide any quantitative information about the safety margin available against the occurrence of failure. In this regard, Goh and Zhang (2012) employed machine learning techniques and finite element (FE) analyses to develop enhanced stability charts that provide a safety factor (SF) value as a quantitative estimate of the stability. However, the authors did not validate the tool against field data, and the applicability of the stability charts is limited to cavity sections located at 100 m depth (i.e., the variability of the overburden thickness has not been included) and characterized by arch-shaped geometries, making the tool unsuitable for quadrangular shapes that represent the most instability-prone geometrical condition.

Mevoli *et al. Geoenvironmental Disasters*   (2024) 11:10

Page 3 of 21

The main purpose of this paper is to provide an advancement of the stability charts proposed by Perrotti et al. (2018) by means of a user-friendly and mechanically-based tool, which allows to estimate a range of safety factor values for an examined cavity section in a straightforward manner. This work firstly describes the procedure to derive the enhanced version of the stability charts, followed by a validation which is proposed by means of their population with a large data-set of three field case studies. Later on, the methodological approach used to estimate the stability of a large number of man-made underground cavities when dealing with preliminary investigations undertaken over a broad area (i.e., urban scale) is described. Finally, a discussion and concluding remarks are presented.

Procedure to enhance the stability charts
FEM-based stability charts
In 2018, Perrotti and co-authors proposed the use of mechanically-based stability charts for a preliminary stability assessment of cavities in soft calcarenite rocks. The corresponding work shows three FEM-based stability charts, each related to a specific value of the Hoek-Brown (HB) parameter m_i (3, 8, 16), which here is supposed to be approximately equal to the ratio between the rock uniaxial compressive and the tensile strength, according to Cai (2010). Moreover, each graph displays four threshold stability curves, defined for a specific range of the shape factor, L/h, which are the result of a large set of parametric finite element analyses performed with Plaxis 2D (Perrotti et al. 2018). The parametric study was aimed at identifying threshold conditions for cave failure in terms

of correlations between geometrical features of the cavities and material geomechanical parameters, taking into account four main hypotheses: plane-strain conditions, intact rock (Geological Strength Index, GSI = 100), HB disturbance factor (D) equal to zero and rectangular-shaped ideal cavity sections. In the FE analyses, the behavior of the intact rock mass is described by an elastic-perfectly plastic constitutive model with a HB failure criterion (Hoek and Brown 1997; Hoek and Martin 2014). Therefore, for each combination of geometrical parameters corresponding to width, L, height, h, and overburden thickness, t, of the ideal cavity section (Fig. 1a), whose values fall in the ranges typically observed for the man-made cavities in the Southern Italian regions, the authors have identified the ultimate value of the uniaxial compressive strength, σ_{cmin}, corresponding to failure conditions. All the analyses were performed assuming drained conditions and no pore water pressure existing within the rock mass, since the caves have been always built above the water level.

The final outcomes of the numerical investigations have been summarized into charts reporting on x-axis the ratio between the width, L, and overburden thickness, t, on y-axis the ratio between the ultimate value of the uniaxial compressive strength, σ_{cmin}, and the vertical stress, σ_v, calculated at depth of the roof of the cavity. When the geometrical and geomechanical information relative to a real case are provided, the corresponding point on the graph, representative of the state of the cavity at the specific cross-section, allows to assess the eventual proneness to failure of the cave (Perrotti et al. 2019). Therefore, if the point is located above the failure curve,
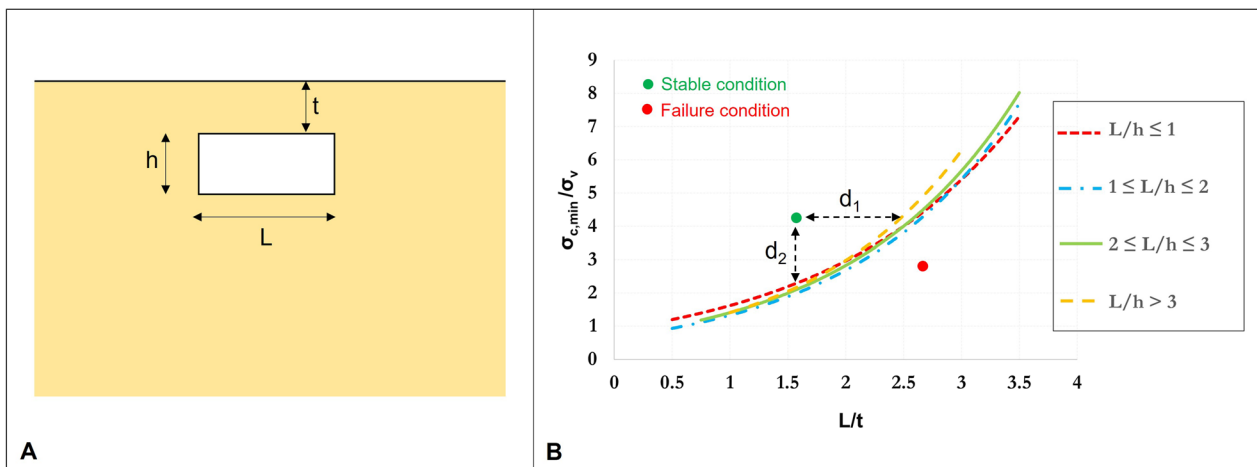

Fig. 1 **a** Geometrical features of the ideal cavity section; **b** stable and failure conditions depicted on the stability chart developed by Perrotti et al. (2018), where: L is the section width; h is the section height; t is the roof thickness; σ_v is the vertical stress at the cavity section depth; σ_{cmin} is the ultimate value of the uniaxial compressive strength of the rock mass; d_1 is the horizontal distance from the failure curve; d_2 is the vertical distance from the failure curve

Mevoli *et al. Geoenvironmental Disasters* (2024) 11:10

Page 4 of 21

the cavity section is supposed to be stable, whereas if the point either belongs to the failure curve or lies below, the cavity section should be considered as highly prone to failure or already collapsed (Fig. 1b). In the graph, starting to the green point (stable condition), an unstable condition can be reached with: a) an increase of the geometrical ratio L/t (d$_1$) corresponding to the enlargement of the section (increase of L for lateral enlargement, decrease of t for upward enlargement); b) a decrease of the ordinate (d$_2$) that corresponds to a decrease of the uniaxial compressive strength (e.g., due to water-induced weakening processes) of the material or an increase of the vertical stress (e.g., due to a load application at the ground level). Anyway, although ratios on x- and y- axis can be identified as safety margins from a stress or geometrical point of view, respectively, these charts do not provide a quantitative estimate of stability.

Stability chart conversion
In order to upgrade the aforementioned stability charts, a quantitative assessment of the cave stability has been integrated through the computation of a range of SF, which is defined as the ratio between the available strength against the occurrence of a general failure mechanism of the whole rock system and the mobilized one. Plaxis 2D allows computing the safety factor value by means of the well-known strength reduction method (Matsui and San 1992), using either the Mohr-Coulomb (MC) failure criterion or the HB one (Plaxis 2020). However, since the SF value obtained with the HB failure criterion used in the version of the charts proposed by Perrotti et al. (2018) resulted to be highly sensitive to the numerical settings of the calculation, the SF computation has been pursued selecting the MC failure criterion for the rock mass. To this purpose, the conversion of the FEM-based stability charts developed by Perrotti et al. (2018) to equivalent MC-based ones has represented a necessary step to develop the enhanced stability charts. To this purpose, a Python code has been developed in the Plaxis 2D editor (SciTE, version 21.01.00.479, Plaxis 2020) aimed at relating the MC strength parameters (c', ϕ') to the HB ones (a, m$_b$, s), according to the well-known equivalence equations proposed by Hoek et al. (2002):

$$\phi' = \sin^{-1}\left[\frac{6am_b(s + m_b\sigma'_{3n})^{a-1}}{2(1+a)(2+a) + 6am_b(s + m_b\sigma'_{3n})^{a-1}}\right] \tag{1}$$

$$c' = \frac{\sigma_{ci}[(1+2a)s + (1-a)m_b\sigma'_{3n}](s + m_b\sigma'_{3n})^{a-1}}{(1+a)(2+a)\sqrt{1 + \frac{6am_b(s+m_b\sigma'_{3n})^{a-1}}{(1+a)(2+a)}}} \tag{2}$$

The HB strength parameters (a, m$_b$, s) are known to depend on the Geological Strength Index, GSI, the disturbance factor, D, and the HB parameter m$_i$. The value of the stress, σ'_{3n}, is expressed as the ratio between the maximum confining stress, σ'_{3max}, and the uniaxial compressive strength for the intact rock mass, σ_{ci}. Specifically, Hoek et al. (2002) suggest the following equation for the computation of the σ'_{3max}, in case of tunnels:

$$\sigma'_{3max} = 0.47\sigma'_{cm}\left(\frac{\sigma'_{cm}}{\gamma H}\right)^{-0.94} \tag{3}$$

where γ is the rock mass unit weight and H is the tunnel depth with respect to the ground level. Moreover, they also suggest to use the value of the confining stress σ'_{3n} instead of the γH parameter, when the first is larger than the second one. In this paper, the coefficient of the earth pressure at rest, K$_0$, is considered to be equal to unity, so that the Eq. 3 has been implemented as it is. In order to proceed with the equivalence between the Hoek-Brown strength envelope and the Mohr-Coulomb one, the global uniaxial compressive strength of the rock mass, σ'_{cm}, needs to be calculated by means of the following expression (Hoek et al. 2002):

$$\sigma'_{cm} = \frac{\sigma_{ci}(m_b + 4s - a(m_b - 8s))\left(\frac{m_b}{4} + s\right)^{a-1}}{2(1+a)(2+a)} \tag{4}$$

Finally, the tensile strength is calculated as:

$$\sigma_t = -s\frac{\sigma_{ci}}{m_b} \tag{5}$$

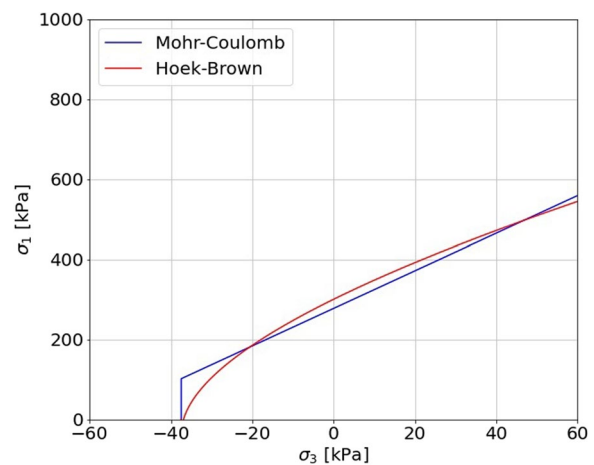which is used as tension cut-off in the numerical model. Figure 2 shows an example of the equivalence between

Fig. 2 Example of the equivalence between HB and MC failure criteria, where σ_1 is the major principal stress and σ_3 is the minor principal stress

the HB and MC failure envelopes, when adopting the procedure proposed by Hoek et al. (2002).

The flow-chart of the Python code shows all the steps required to get the MC-based stability charts (Fig. 3). The geometry of the numerical model is first built by identifying three rectangular areas representing the overall rock domain, an area surrounding the cavity where a mesh refinement is performed and the cavity section, respectively (Fig. 4). While the size of the cavity section changes according to the parametric approach, the other two domains keep constant geometries. A very fine mesh with 15-noded triangular elements has been applied, with major refinement in the area surrounding the cavity. This choice reflects the need for proper calculation accuracy for a better failure mechanism detection with convenient computational time. The adopted mechanical boundary conditions are represented by rollers at the lateral sides of the rock domain, fixed constraints at the bottom, and free boundary at the ground level. Subsequently, a first trial value of the uniaxial compressive strength is chosen, and the equivalent MC strength parameters are then computed. Table 1 lists the values of the physical properties and mechanical parameters used in the numerical model, corresponding to typical values of the calcarenite outcropping in Southern Italy (Coviello et al. 2005; Andriani and Walsh 2010; Ciantia et al. 2015). The GSI value is considered to be equal to 100 in order to satisfy the hypothesis of intact rock mass, whereas the parameter D, representative of the disturbance factor induced by the excavation technique, is set equal to 0 (typically the hand-excavation technique was adopted and the rock mass has not been disturbed or affected by stress release processes, as mentioned in Perrotti et al. (2019). The following three stages of the mechanical analysis have been performed:

1. Initial stress state computation with K_0 procedure;
2. elasto-plastic stress–strain analysis with no excavation;
3. elasto-plastic stress–strain analysis with a single excavation step of cavity, where displacements resulting from the previous step have been reset.

Since no clear information on the in situ actual excavation sequence was available, the adopted single excavation stage represents a conservative assumption. In order to identify the value of the uniaxial compressive strength mobilized at failure, the lack of numerical convergence returned by the second elasto-plastic stress–strain analysis at failure conditions, as provided by the
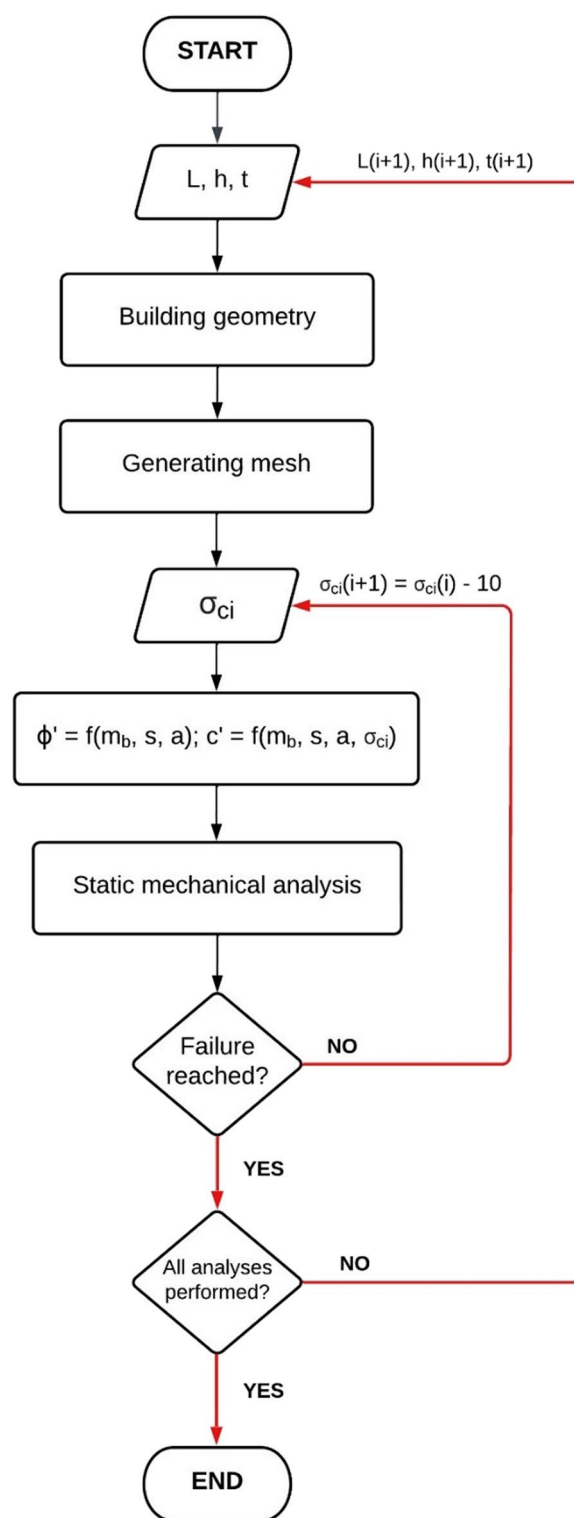

Fig. 3 Flow-chart of the Python code for Plaxis 2D analysis automation

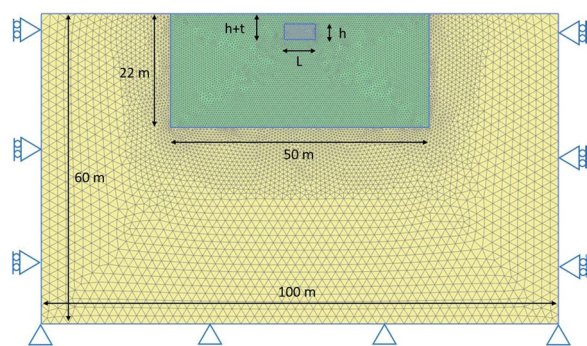Mevoli *et al. Geoenvironmental Disasters*   (2024) 11:10

Page 6 of 21

Fig. 4 Discretization mesh adopted for the numerical model. Boundary conditions: rollers at the lateral borders and fixed constraints at the base of the domain

Table 1 Physical and mechanical parameters of the rock used in the numerical analyses

Parameter	Value
Unit weight, γ (kN/m^3)	15.5
Coefficient of earth pressure at rest, K_0 (-)	1
Young's modulus, E (kPa)	1×10^5
Poisson ratio, ν (–)	0.3
Uniaxial compressive strength, σ_{ci} (kPa)	Variable
Geological Strength Index, GSI (–)	100
Disturbance factor, D (–)	0
Hoek-Brown parameter m_i (–)	3, 8, 16

Python code, has been considered. Details regarding the criteria for detecting the cave failure from a numerical point of view are reported in Perrotti et al. (2018). Therefore, when convergence is guaranteed, the routine is prosecuted with a reduced value of σ_{ci} until lack of convergence is reached. A decrease for σ_{ci} equal to 10 kPa is applied between step *i* and *i+1*. At this stage, a new numerical investigation begins for a different combination of geometrical parameters (L, h, and t) of the cave section. Finally, all the results of the numerical analyses have been summarized in MC-based failure curves, whose trend is described by a 3rd order polynomial equation (Fig. 5).

Enhanced stability charts: iSUMM

For the enhanced MC-based stability charts, a large set of ideal sections has been selected and the corresponding SF value has been calculated. The SF computation is achieved by adding a safety factor phase after the second elasto-plastic stress–strain analysis. It is worthwhile pointing out that a safety factor stage performs

the progressive reduction of the shear strength and tensile strength parameters until failure occurs, according to the following equation:

$$SF = \frac{\tan \phi'_f}{\tan \phi'_m} = \frac{c'_f}{c'_m} = \frac{\sigma_{tf}}{\sigma_{tm}} = M_{sf} \tag{6}$$

where the subscripts f and m stand for failure and mobilized parameters, respectively (Plaxis 2020). M_{sf} is the total multiplier provided by the Plaxis load advancement algorithm and corresponds to the SF value. Therefore, once the failure mechanism is fully developed due to the strength parameter reduction and the safety phase ends, the corresponding value of total multiplier, M_{sf}, is stored as SF.

Figure 6 shows the states of the investigated ideal sections within the stability charts (blue circles), with their corresponding computed SF values. Once the values of L/h and L/t were established, the σ_{ci} was varied in order to get equally-spaced points in the vertical direction above the failure curve. For example, for the line of points corresponding to L/t equal to 3, the uniaxial compressive strength was varied of 165 kPa for the $1 < L/h \leq 2$ sub-case of the $m_i = 3$ stability chart. Subsequently, a series of FE analyses were performed to get the associated SF, whose values are shown near the corresponding point in Fig. 6. In this way, it was possible to extrapolate the curves for specific values of SF. Each SF curve can be described by a third-order polynomial equation, leading to the final version of the enhanced stability charts (Figs. 7, 8 and 9). Considering that Perrotti et al. (2018) provided three FEM-based stability charts for the various HB parameter m_i values, and that four sub-categories of the shape factor, L/h, have been accounted for each of them, a total of twelve enhanced stability sub-plots have been derived in this study. Each colored area above the failure curve (SF = 1) identifies a specific SF range for which the safety factor of an examined case can be quantitatively estimated.

Validation and application to case studies
Validation

The enhanced version of the stability charts has been validated against field data collected from 35 underground cavities located in Southern Italy: 19 in Massafra, 18 in Canosa di Puglia and 1 in Marsala. The validation process is outlined in Fig. 10 and comprises three main phases. In the preliminary stage, all pertinent information, including geometric features and geomechanical properties as detailed in Section "Proposed methodology", is collected to enable the next steps. Later on, the enhanced Stability Charts (SC) are employed to determine the range of safety factor values, SF_{SC}, associated with the
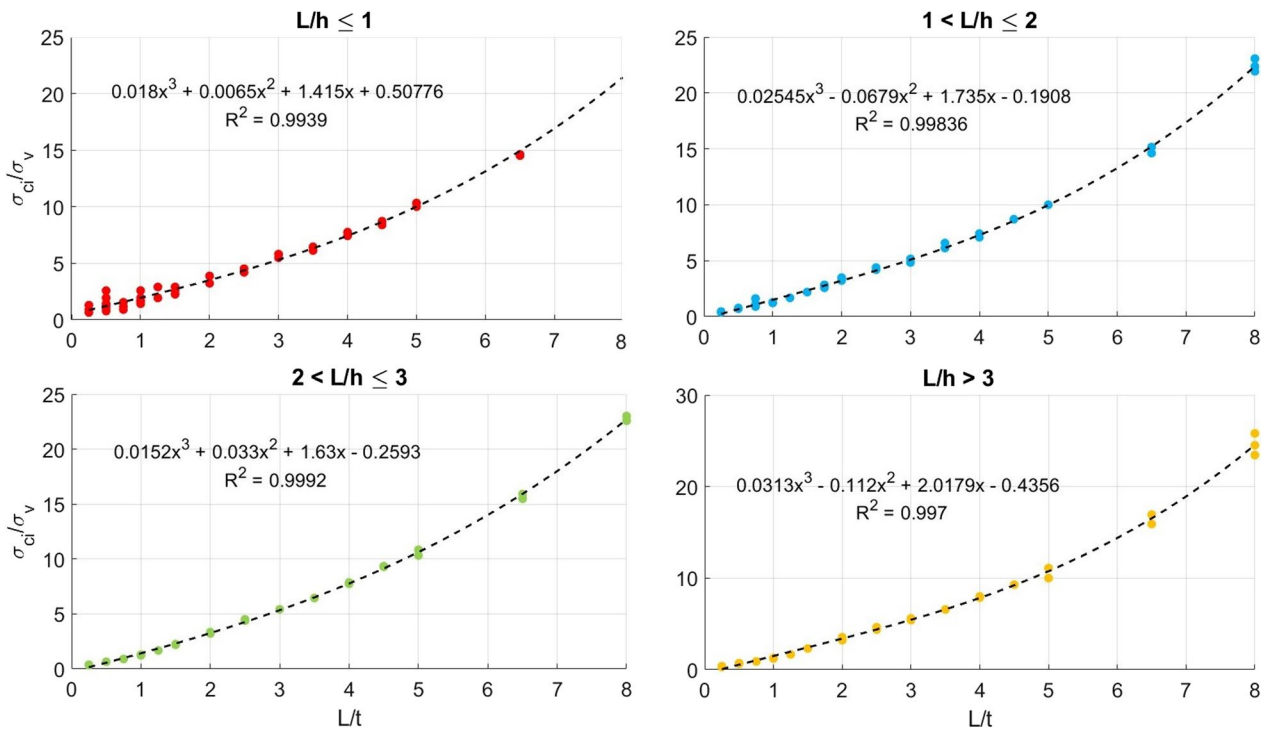
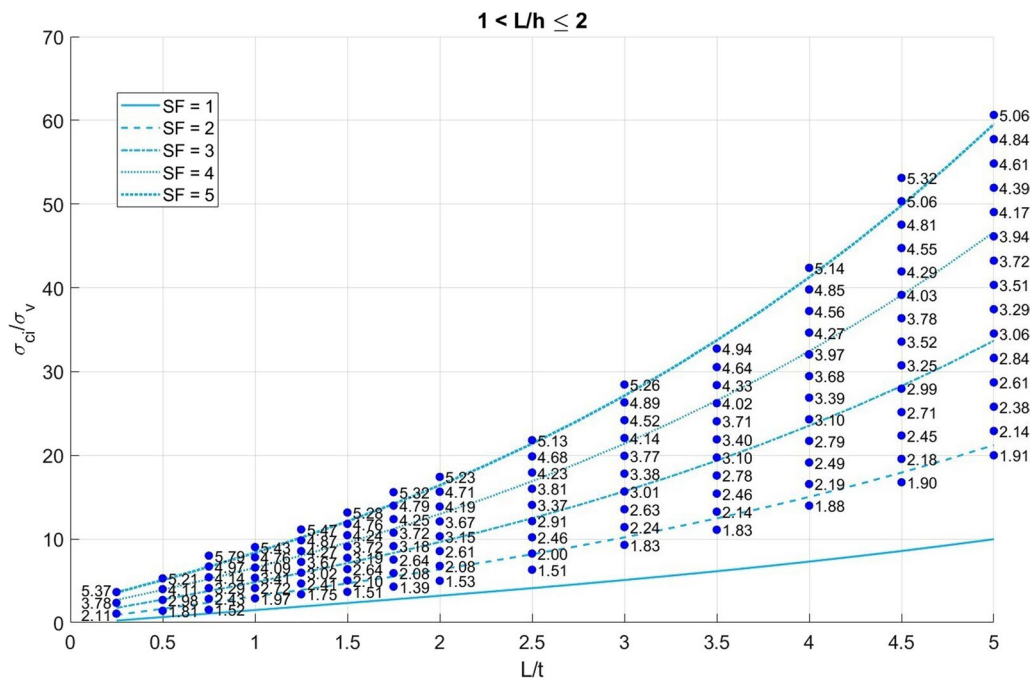**Fig. 5** MC-based failure envelopes for $m_i = 3$

Fig. 6 Extrapolation of the SF curves for the $m_i = 3$ stability chart and $1 < L/h \leq 2$ sub-case

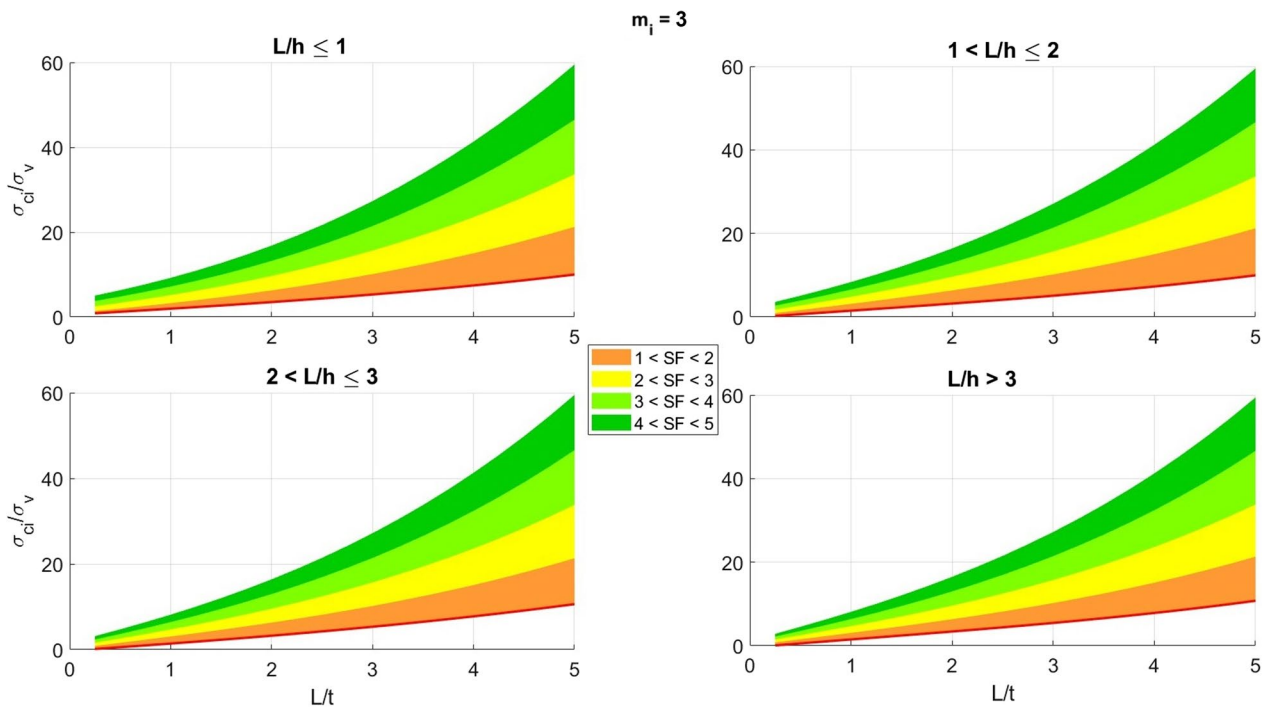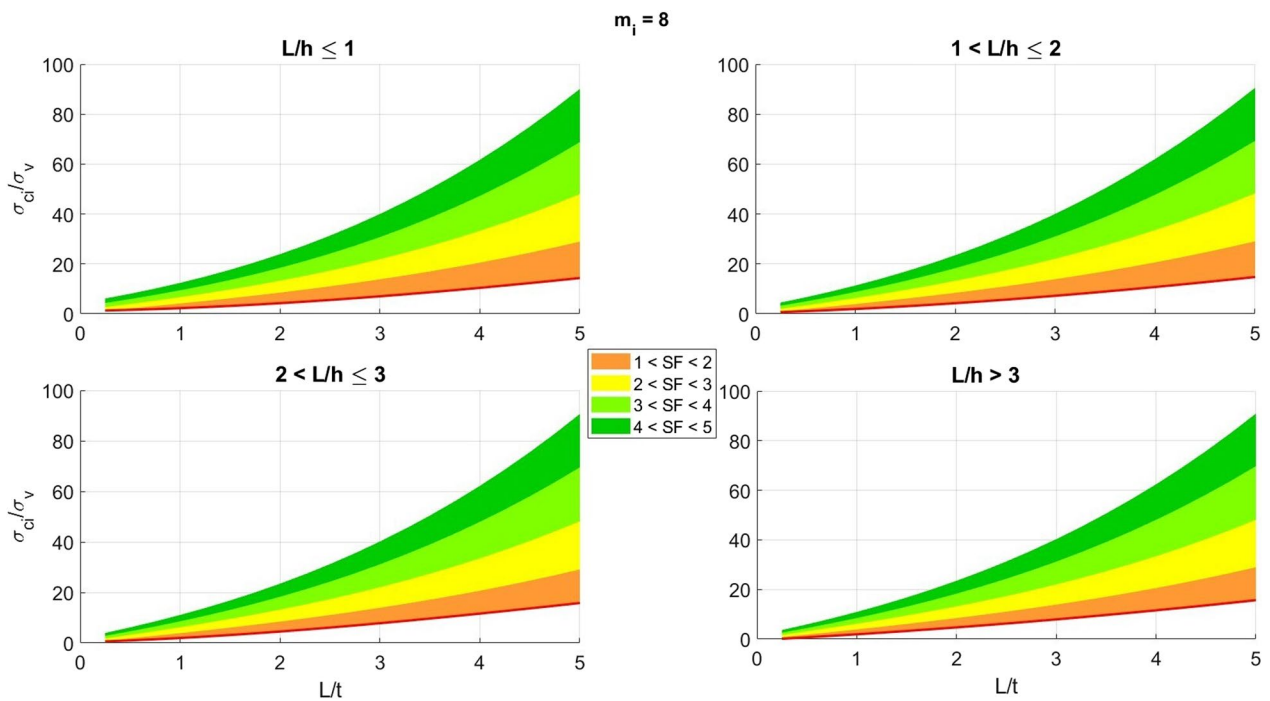Mevoli *et al. Geoenvironmental Disasters*   (2024) 11:10

Page 8 of 21

Fig. 7 Enhanced stability chart for $m_i = 3$ case with the four sub-categories depending on the assumed L/h value

Fig. 8 Enhanced stability chart for $m_i = 8$ case with the four sub-categories depending on the assumed L/h value

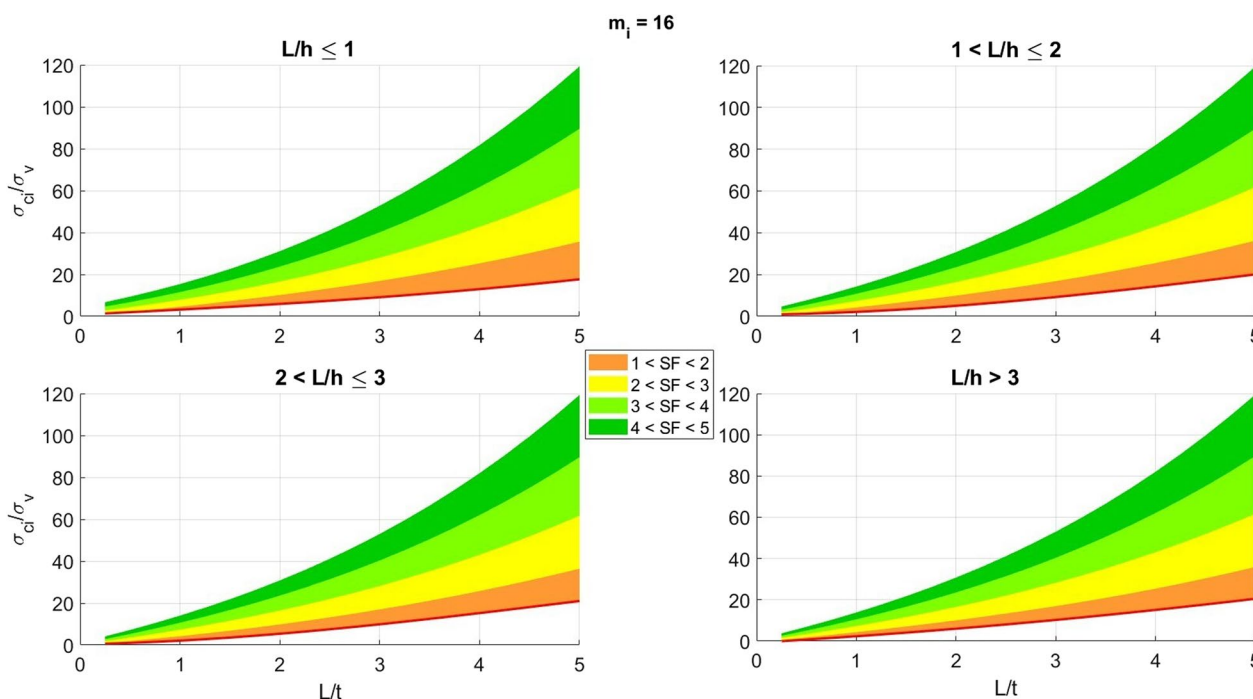Mevoli *et al. Geoenvironmental Disasters*   (2024) 11:10

Page 9 of 21

Fig. 9 Enhanced stability chart for $m_i = 16$ case with the four sub-categories depending on the assumed L/h value

representative point of the cavity. This is followed by conducting 2D finite element analyses that aim to assess the stability conditions by assuming the real section of the caves (advanced stage), whose shape may be different from the rectangular one, and thereby establish the real 2D safety factor, SF_R. The reliability of the methodology is assessed through comparing the two SF values. When SF_R is equal to or greater than the upper limit of the SF_{SC}, the enhanced stability charts function correctly, and this represents a conservative condition.

Application to case studies
Canosa di Puglia
Relevant information about subsurface environments was acquired by consulting an existing archive provided by the Canosa di Puglia Municipality. Some examples of the total amount of 47 underground systems that met the applicability hypotheses of the enhanced stability charts, are here reported (18 cases). The hypogenous environments are characterized by sections of various shapes: rectangular, trapezoidal, pointed arch, round arch, etc. Table 2 summarizes the procedural steps to follow for the direct application of the enhanced stability charts corresponding to $m_i = 3$. Here, the vertical surcharge, $\Delta\sigma_v$, can be represented, in few cases, by a shallow clay layer overlaying the rock stratum whose total unit weight is 19 kN/m^3 (Mastropasqua and Laghezza 2009), and/or a

building at the ground surface. In this latter case, the vertical load contribution is assumed equal to 10 kPa/floor for reinforced concrete and 14 kPa/floor for load-bearing masonry. Figures 11 and 13 show respectively the stability assessment of 11 rectangular real sections pertaining to the $1 < L/h \leq 2$ shape factor category, and an example of application to 6 sections with shapes other than rectangular (Fig. 12).

In order to validate the enhanced stability charts, FE numerical analyses were conducted in Plaxis 2D to obtain SF_R. Table 3 lists the physical properties and mechanical parameters of the calcarenite rock outcropping in the area, according to the work published by Castellanza et al. (2018) and Perrotti et al. (2018). The values taken into consideration are those relating to saturated conditions that correspond to the worst-case scenario for the stability. An elastic-perfectly plastic behavior is assumed for the rock mass, with an equivalent Mohr-Coulomb failure envelope derived from the HB parameters listed in Table 3. The resulting SF_R values are provided in Table 2 and in Figs. 11 and 13 next to the corresponding points. It is possible to notice that, in the majority of the analyzed cases, the representative point of the section falls into the expected range, except for four cases. Although the calculated SF_R does not lie within the expected SF_{SC} range, the application of the enhanced stability charts would be conservative.
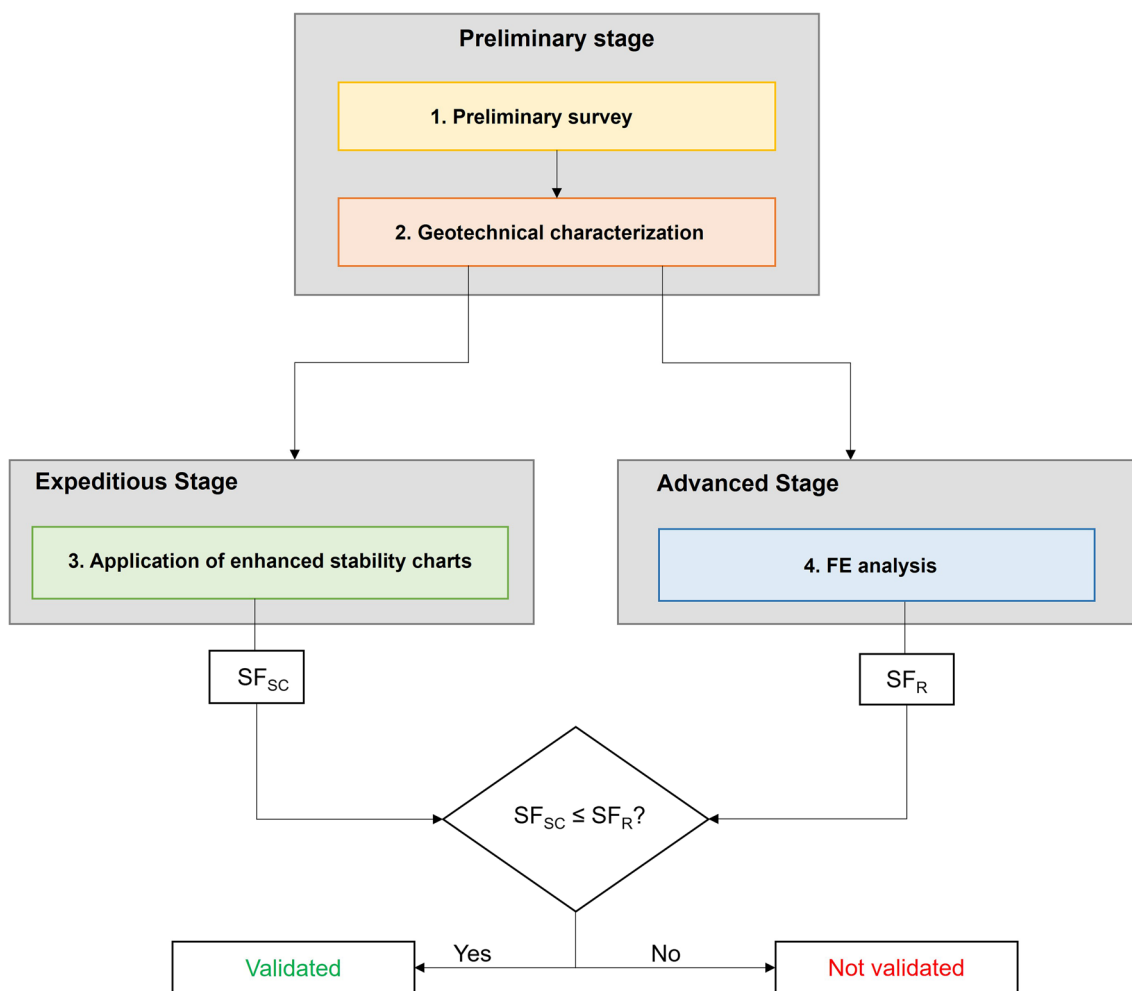
Fig. 10 Scheme of the validation procedure

Massafra

A total of 19 hypogenous systems have been selected out of the 50 registered in the available database, which are typically characterized by a series of rooms and corridor environments with mainly rectangular sections. The enhanced stability charts have been applied on 24 real rectangular sections, whose parameters are listed in Table 4. During in-situ measurements, information about the geometrical dimensions and the vertical surcharge acting on them was collected, which is primarily represented by reinforced concrete or load-bearing masonry buildings. The physical properties and mechanical parameters of the rock mass were measured through laboratory tests performed on rock samples collected in the area of study. The resulting values demonstrate the existence of two distinct sedimentary lithofacies in the area: one coarse-grain type that is very friable and irregularly cemented, characterized by lower strength (Facies A), and the second that is well-cemented, with

lower permeability and higher strength (Facies B; Andriani and Walsh 2010). Figure 14 shows an example of stability assessment for those sections belonging to the $2 < L/h \leq 3$ sub-category of the enhanced stability chart corresponding to the $m_i = 3$ parameter. The direct application is then validated against the SF values calculated from FE numerical analyses that use the parameters listed in Table 5. Firstly, the representative point of the section lies within the expected range in the majority of the examined cases, except for section No. 1 of cavity No. 18 (Table 4), for which the computed SF is slightly greater than the values comprised in the expected range ($3 < SF < 4$). Secondly, the point located on the failure curve ($SF = 1.14$) suggests a case at risk. In fact, according to the local news, the worsening of Buona Nuova Crypt structural conditions (a nearby cavity already precarious after the roof collapse occurred in September 2017) was documented on the 11th February 2021, just a few months after the in-situ surveys. Consequently, the

Table 2 List of geometrical characteristics, stress parameters and SF values for every rectangular real section

Cavity code	Sec.	L (m)	h (m)	t (m)	L/t (–)	L/h (–)	$\Delta\sigma_v$ (kPa)	σ_v (kPa)	σ_{ci}/σ_v (–)	SF_{SC} (–)	SF_R (–)	$SF_{SC} \le SF_R$?
Rectangular sections												
CP_Cav9	1	2.67	3.94	5.74	0.47	0.68	28.00	119.84	4.17	3 < SF < 4	3.94	Yes
CP_Cav12	1	7.17	4.80	7.94	0.90	1.49	14.00	141.04	3.55	2 < SF < 3	2.64	Yes
CP_Cav25	1	4.39	2.53	9.51	0.46	1.74	106.60	258.76	1.93	2 < SF < 3	2.76	Yes
CP_Cav39	1	2.57	6.00	9.85	0.26	0.43	28.00	185.60	2.69	3 < SF < 4	3.11	Yes
	2	3.14	6.17	9.16	0.34	0.51	20.00	166.56	3.00	3 < SF < 4	3.11	Yes
CP_Cav54	1	2.43	3.40	7.65	0.32	0.71	28.00	150.40	3.32	3 < SF < 4	3.97	Yes
CP_Cav60	1	4.90	1.76	11.02	0.44	2.78	28.00	204.32	2.45	3 < SF < 4	3.30	Yes
	2	6.49	5.66	7.80	0.83	1.15	14.00	138.80	3.60	2 < SF < 3	2.77	Yes
CP_Cav62	1	4.32	5.80	12.10	0.36	0.74	20.00	213.60	2.34	2 < SF < 3	2.80	Yes
CP_Cav63	1	4.05	3.82	10.60	0.38	1.06	28.00	197.60	2.53	3 < SF < 4	3.20	Yes
CP_Cav68	1	4.12	4.50	7.08	0.58	0.92	0.00	113.28	4.41	3 < SF < 4	3.75	Yes
	2	3.08	3.56	7.62	0.40	0.87	14.00	135.92	3.68	3 < SF < 4	3.90	Yes
CP_Cav69	1	4.00	3.00	9.08	0.44	1.33	0.00	145.28	3.44	3 < SF < 4	3.80	Yes
CP_Cav70	1	5.70	2.96	4.53	1.26	1.93	0.00	72.48	6.90	3 < SF < 4	3.40	Yes
CP_Cav73	1	3.58	1.59	10.67	0.34	2.25	0.00	170.72	2.93	4 < SF < 5	4.23	Yes
	2	3.70	2.20	12.46	0.30	1.68	14.00	213.36	2.34	3 < SF < 4	3.40	Yes
CP_Cav74	1	3.46	1.89	10.15	0.34	1.83	0.00	162.40	3.08	**3 < SF < 4**	**4.23**	Yes
CP_Cav76	1	4.07	4.02	6.02	0.68	1.01	14.00	110.32	4.53	3 < SF < 4	3.76	Yes
CP_Cav78	1	8.31	4.49	8.56	0.97	1.85	0.00	136.96	3.65	2 < SF < 3	2.52	Yes
	2	3.30	2.53	13.16	0.25	1.30	0.00	210.56	2.37	3 < SF < 4	3.80	Yes
Other shapes												
CP_Cav5	1	7.35	6.77	11.51	0.64	1.09	28.00	212.16	2.36	2 < SF < 3	2.41	Yes
	2	7.05	6.34	8.25	0.85	1.11	28.00	160.00	3.13	2 < SF < 3	2.66	Yes
CP_Cav9	2	2.89	5.76	3.57	0.81	0.50	56.00	113.12	4.42	3 < SF < 4	3.30	Yes
	3	3.15	4.24	2.09	1.51	0.74	28.00	61.44	8.14	**3 < SF < 4**	**4.34**	Yes
CP_Cav15	1	5.76	3.07	10.82	0.53	1.88	30.00	203.12	2.46	**2 < SF < 3**	**3.04**	Yes
CP_Cav24	1	7.33	6.78	3.49	2.10	1.08	14.00	69.84	7.16	**2 < SF < 3**	**3.12**	Yes

The bold data refer to cases in which the numerical result does not fall into the expected SF range
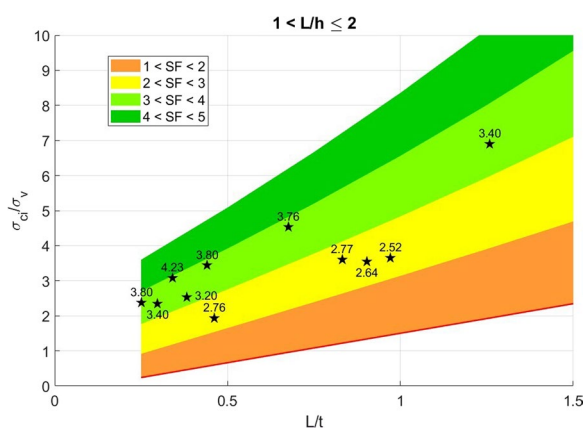

Fig. 11 Graph corresponding to $1 < L/h \le 2$ category of the $m_i = 3$ enhanced stability chart: stability assessment of 11 rectangular real sections with corresponding computed SF values

entrance to the area was banned for the next two years until the recent reopening on the 25th February 2023 after safety works. Even if cavity No. 18 was not involved in collapse phenomena, the outcome indicates precarious structural conditions that need to be properly addressed, given the history of instabilities in the area.

Marsala

In June 2011, an emblematic sinkhole event occurred in the eastern area of the city at an underground cavity where signs of instability were already noted during a previous in-situ survey conducted in 2000. At that time, occurrences of falls and rock failures were localized in the eastern zone of the quarry, whose environments were characterized by thin rock pillars and narrow walls separating wider spaces (Bonamini et al. 2013; Fazio
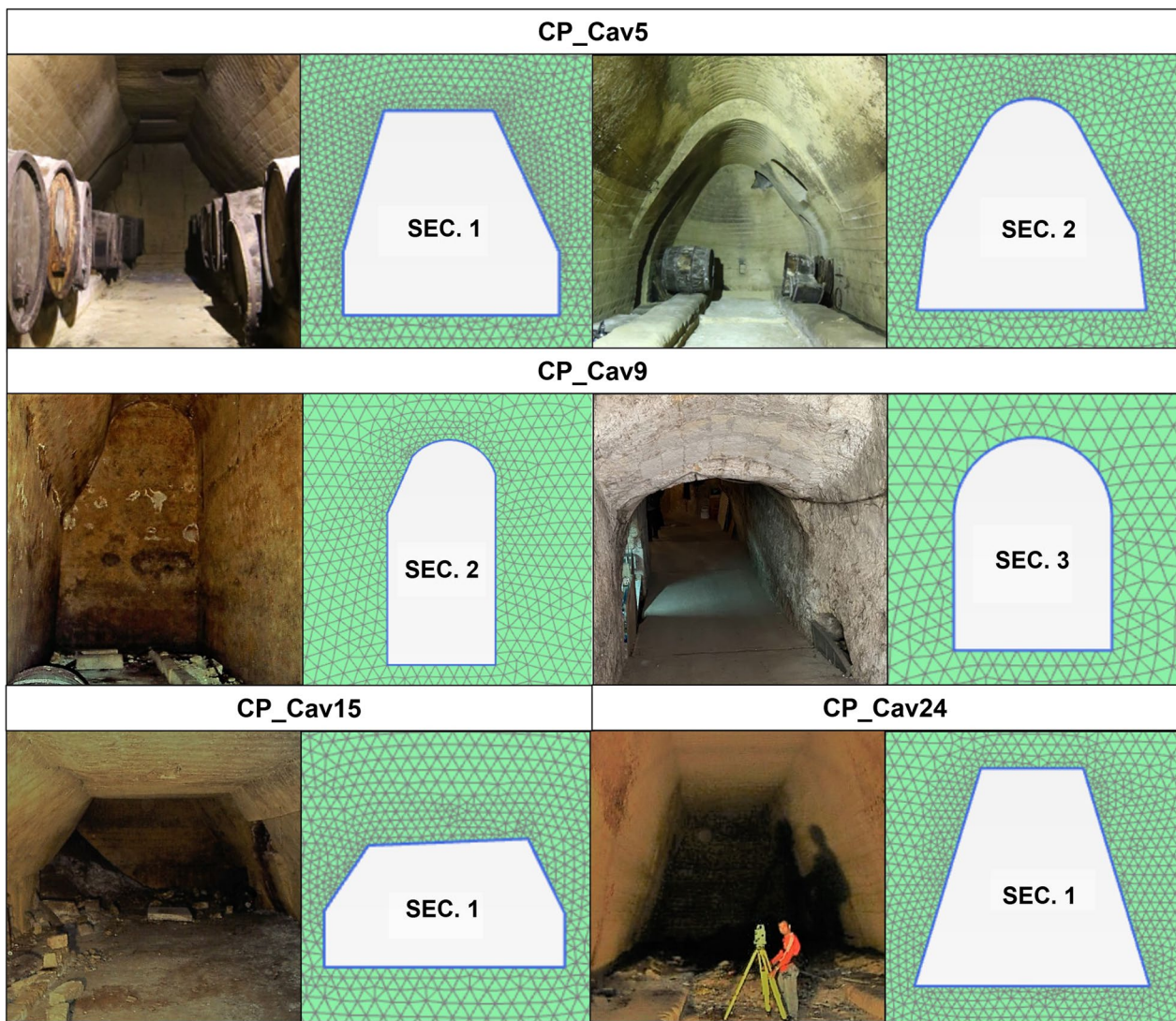
Fig. 12 Typology of sections with a shape different from the rectangular one observed in the Canosa di Puglia area

Table 3 Physical properties and mechanical parameters of the calcarenites outcropping in Canosa di Puglia used in the FE analyses

Parameter	Value
Unit weight, γ (kN/m³)	16.00
Coefficient of earth pressure at rest, K_0 (–)	1
Young's modulus, E (kPa)	116×10^3
Poisson ratio, ν (–)	0.3
Uniaxial compressive strength, σ_{ci} (kPa)	500
Geological Strength Index, GSI (–)	100
Disturbance factor, D (–)	0
Hoek-Brown parameter m_i (–)	3

et al. 2017; Perrotti et al. 2019). After the 2011 collapse, a thorough topographic investigation revealed an elliptical sinkhole with a maximum diameter of about 40 m, and a minimum of about 25 m (Fig. 15). Instability phenomena firstly developed in highly stressed pillars, whose progressive failure resulted in cracking propagation up to the ground surface causing subsidence (Fazio et al. 2017). Rectangular-shaped environments with variable dimensions characterize the cavity system, with average height of 2.7 m (1.1–7.5 m), average width of 3.5 m (1.8–8 m), average length of 12 m (2.6–40 m), and a roof thickness ranging between 8.2 and 11.8 m.
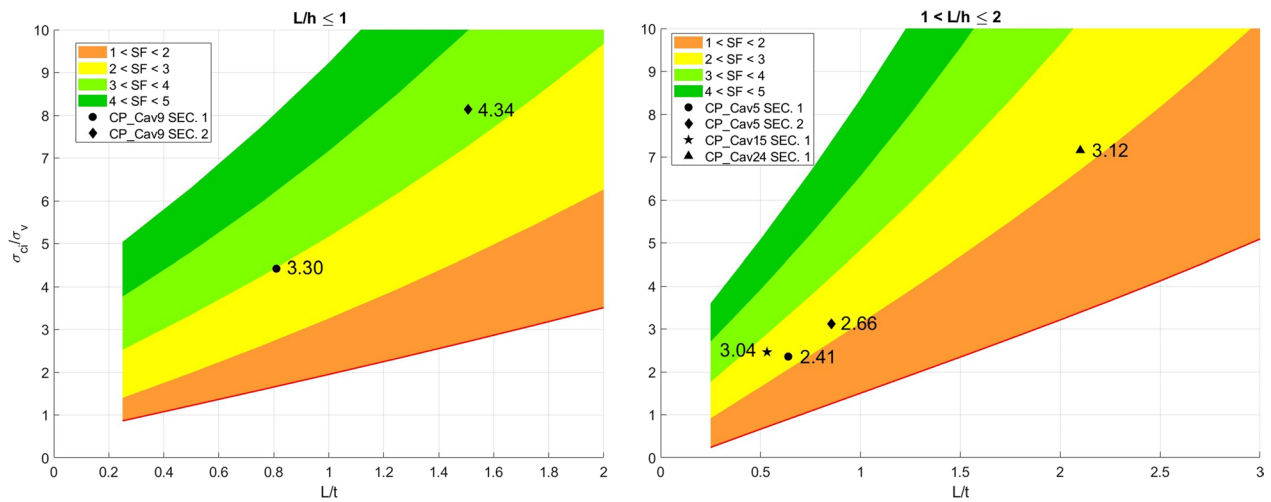
Fig. 13 Application of the enhanced stability charts to real sections with shapes other than rectangular

Table 4 List of geometrical characteristics, stress parameters and SF values for every rectangular real section

Cavity code	Sec.	L (m)	h (m)	t (m)	L/t (–)	L/h (–)	$\Delta\sigma_v$ (kPa)	σ_v (kPa)	σ_{ci}/σ_v (–)	SF_{SC} (–)	SF_R (–)	$SF_SC \le SF_R$?
M_ANT_01	1	7.30	2.66	2.00	3.65	2.74	68.00	105.78	6.52	1 < SF < 2	1.14	Yes
	2	3.69	2.66	2.00	1.85	1.39	0.00	37.78	18.26	SF > 5	5.94	Yes
M_ANT_03	1	3.63	2.50	3.70	0.98	1.45	0.00	69.89	9.87	SF > 5	5.96	Yes
	2	3.23	2.00	3.20	1.01	1.62	0.00	60.45	11.41	SF > 5	6.72	Yes
	3	5.53	2.35	3.20	1.73	2.36	0.00	60.45	11.41	4 < SF < 5	4.00	Yes
M_ANT_04	1	3.98	3.20	3.00	1.33	1.24	14.00	70.67	9.76	4 < SF < 5	4.68	Yes
M_ANT_06	1	3.50	1.80	5.00	0.70	1.94	0.00	94.45	7.31	SF > 5	6.00	Yes
M_ANT_07	1	4.50	2.20	2.00	2.25	2.05	0.00	37.78	18.26	4 < SF < 5	4.88	Yes
M_ANT_08	1	6.00	2.40	5.00	1.20	2.50	0.00	94.45	7.31	3 < SF < 4	3.80	Yes
M_ANT_09	1	4.60	2.50	2.00	2.30	1.84	0.00	37.78	18.26	4 < SF < 5	4.75	Yes
M_ANT_12	1	8.30	2.30	5.00	1.66	3.61	0.00	94.45	7.31	2 < SF < 3	2.68	Yes
M_ANT_13	1	4.10	2.13	0.70	5.86	1.92	0.00	13.22	52.18	3 < SF < 4	3.63	Yes
M_ANT_14	1	3.90	2.40	2.00	1.95	1.63	0.00	37.78	18.26	SF > 5	5.58	Yes
M_ANT_15	1	4.00	2.60	2.00	2.00	1.54	0.00	37.78	18.26	SF > 5	5.46	Yes
M_ANT_16	1	5.10	2.30	2.00	2.55	2.22	30.00	67.78	10.18	2 < SF < 3	2.53	Yes
M_ANT_17	1	5.20	2.10	2.00	2.60	2.48	30.00	67.78	10.18	2 < SF < 3	2.48	Yes
M_ANT_18	1	4.50	2.50	5.00	0.90	1.80	30.00	124.45	5.54	**3 < SF < 4**	**4.05**	Yes
M_ANT_19	1	5.46	3.31	10.00	0.55	1.65	0.00	196.40	8.76	SF > 5	7.94	Yes
M_ANT_20	1	6.45	3.14	1.20	5.38	2.05	28.00	51.57	33.35	2 < SF < 3	2.76	Yes
	2	9.21	2.79	1.20	7.68	3.30	0.00	23.57	72.98	2 < SF < 3	2.94	Yes
M_ANT_22	1	4.97	2.64	8.00	0.62	1.88	28.00	179.12	3.85	3 < SF < 4	3.84	Yes
	2	10.40	3.76	4.00	2.60	2.77	17.00	92.56	7.45	1 < SF < 2	1.76	Yes
M_ANT_23	1	9.40	3.10	2.00	4.70	3.03	0.00	37.78	18.26	1 < SF < 2	1.97	Yes
M_ANT_33	1	2.93	2.15	1.50	1.95	1.36	0.00	28.34	24.35	SF > 5	7.42	Yes

The bold data refer to cases in which the numerical result does not fall into the expected SF range. M_ANT_19 and M_ANT_20 are caves within the strongest lithofacies (Facies B)
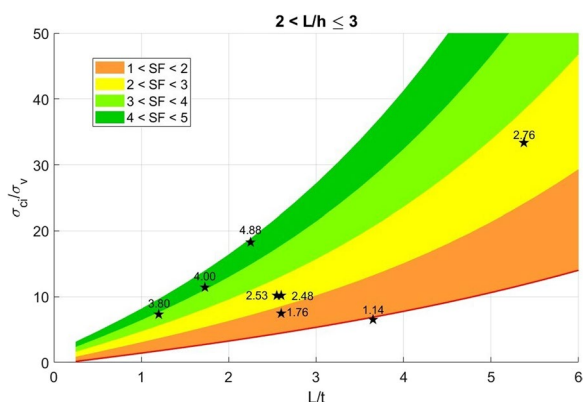
Fig. 14 Graph corresponding to $2 < L/h \leq 3$ category of the $m_i = 3$ enhanced stability chart: stability assessment of 8 rectangular real sections with corresponding computed SF values

Table 5 Physical properties and mechanical parameters of the lithofacies present in Massafra territory

Parameter	Value	
	Facies A	**Facies B**
Unit weight, γ [kN/m^3]	18.89	19.64
Coefficient of earth pressure at rest, K_0 [–]	1	1
Young's modulus, E [kPa]	3.8×10^6	3.8×10^6
Poisson ratio, ν [–]	0.3	0.3
Uniaxial compressive strength, σ_{ci} [kPa]	690	1720
Geological Strength Index, GSI [–]	100	100
Disturbance factor, D [–]	0	0
Hoek-Brown parameter m_i [–]	3	3

The enhanced stability charts are here applied over 5 sections (Table 6), with geometrical dimensions and surcharge information acquired from the 3D model produced by Fazio et al. (2017). The peculiarity of the Marsala cavity environments led to the measurement of section width from wall-to-wall (i.e., entire span), as thin pillars and walls minimally contribute to the structural stability of the system (Fiore et al. 2018). Geomechanical parameters of the Marsala Calcarenite have been determined from geotechnical laboratory tests performed on rock samples retrieved from the inner rooms of the cavity (Zimbardo 2009; Fazio et al. 2017; Perrotti et al. 2019). Table 7 summarizes the values used to compute the ordinate of the Marsala section representative points and to perform numerical computation of the corresponding SF_R. No surcharge acts on the identified sections, which is correlated to free field conditions.

The enhanced stability chart here applied is the one corresponding to the m_i parameter equal to 8 and the $L/h > 3$ sub-category, given that rectangular sections are all characterized by large widths and small heights (Fig. 16). The proximity of Sections 1 and 2 to the failure envelope (SF = 1) confirms instability configurations right within the area characterized by the sinkhole. The numerical-estimated SF_R values validate the locations of the points into the expected SF ranges on the graph. Specifically, the FE analysis performed on Section No. 1 returned no convergence of the second elasto-plastic stress–strain analysis, therefore corresponding to failure conditions (SF = 1). A phenomenological study of the collapse of the Marsala cave has been broadly investigated through a 3D FE modeling (Fazio et al. 2017).

Proposed methodology

A comprehensive methodology for the assessment of the stability of underground cavities is proposed. The scheme shown in Fig. 17 distinguishes four main steps to be addressed:

1. Preliminary survey to collect relevant geometrical data on the caves for the application of the enhanced stability charts;
2. Geotechnical characterization of the rocks present in the study areas;
3. Application of the enhanced stability charts to identify the corresponding SF range and, therefore, the underground cavity sections at risk;
4. Specific FE analyses designed to provide further insights about the resulting stress and strain fields, the corresponding SF value, and the potential failure mechanism, once the calculated SF range results to be relatively low.

The preliminary survey represents the first step to be undertaken in order to gather essential sets of data per cavity regarding the geometrical features of the sections to be studied, the GPS coordinates, characteristics of a potential surcharge acting on the cavity (e.g., pre-existing building, soil layers above the rock stratum accommodating the cavity, etc...), and knowledge about the presence of potential discontinuities. Specifically, the methodology requires to select a set of sections per cavity in accordance with the applicability hypotheses of the stability charts developed by Perrotti et al. (2018): (a) intact rock (GSI = 100); (b) plane-strain conditions; (c) rectangular section; (d) HB disturbance factor, D = 0. To meet the

Mevoli *et al. Geoenvironmental Disasters*   (2024) 11:10

Page 15 of 21

Fig. 15 On the left: topographic survey of the underground quarry before failure, with indication of the sinkhole perimeter (Bonamini et al. 2013). On the right: movements of large volumes of rock along sub-vertical fractures surveyed in 2000 (Vattano et al. 2013)

Table 6 List of geometrical characteristics, stress parameters and SF values of the Marsala cavity sections

Sec.	L (m)	h (m)	t (m)	L/t (–)	L/h (–)	$\Delta\sigma_v$ (kPa)	σ_v (kPa)	σ_{ci}/σ_v (–)	SF_{SC} (–)	SF_R (–)	$SF_{SC} \leq SF_R$?
1	30.00	1.70	9.00	3.33	17.65	0.00	144.00	9.03	1 < SF < 2	1.00	Yes
2	27.50	2.80	8.60	3.20	9.82	0.00	137.60	9.45	1 < SF < 2	1.23	Yes
3	20.20	2.30	8.60	2.35	8.78	0.00	137.60	9.45	1 < SF < 2	1.80	Yes
4	17.50	2.60	10.60	1.65	6.73	0.00	169.60	7.67	2 < SF < 3	2.12	Yes
5	14.00	2.00	9.40	1.49	7.00	0.00	150.40	8.64	2 < SF < 3	2.60	Yes

Table 7 Physical properties and mechanical parameters of the Marsala calcarenite

Parameter	Value
Unit weight, γ [kN/m³]	16.00
Coefficient of earth pressure at rest, K_0 (–)	1
Young's modulus, E([kPa)	300×10^3
Poisson ratio, ν (–)	0.3
Uniaxial compressive strength, σ_{ci} (kPa)	1300
Geological Strength Index, GSI (–)	100
Disturbance factor, D (–)	0
Hoek-Brown parameter m_i (–)	8

first requirement, the location of the section to be studied must be identified where the walls, pillars and roof do not present any discontinuity. Furthermore, the second hypothesis implies that the choice is affected by the geometrical configuration of the underground cavity environments (Fig. 18). In corridor-type rooms, for which the

width, L, over the length, l, ratio is less than or equal to 0.7, the location of the section is chosen as far away from geometrical variations as possible (Fig. 18, Section A). Whereas, in those chambers realized with the *room and pillar* technique, the selection of the location depends on the comparison between the pillar thickness and the span of the room. When the thickness of the pillar, L_p, is less or equal to half of the width of the adjacent voids, L_v, the two separated cavity environments behave as a single system (Fiore et al. 2018), so that the width, L, to be considered is the one that encompasses the entire span (Fig. 18, Section B). On the contrary, the section is chosen between adjacent pillars or between the room wall and the pillar (Fig. 18, Section C). After the identification of the suitable location, the measures of the width, L, the height, h, and the roof thickness, t, are retrieved. All the information to be acquired in this first stage usually requires in-situ surveys or access to an existing database.

The second step of the methodology aims to characterize the geo-materials existing in the studied locations
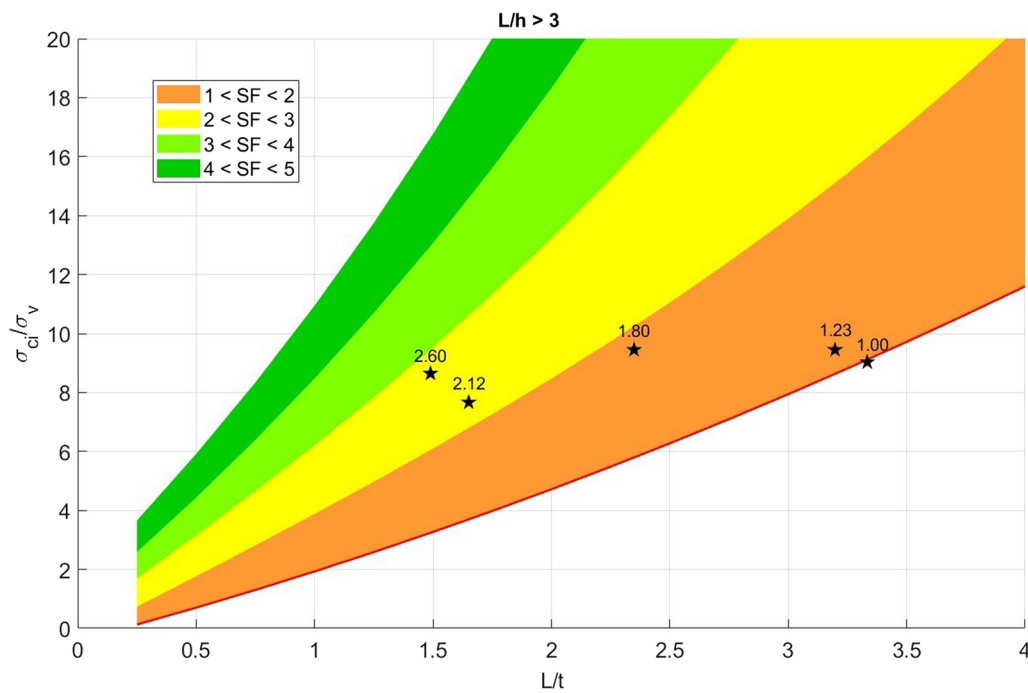
Fig. 16 Graph corresponding to $L/h > 3$ category of the $m_i = 8$ enhanced stability chart: stability assessment of 5 rectangular real sections with corresponding computed SF values
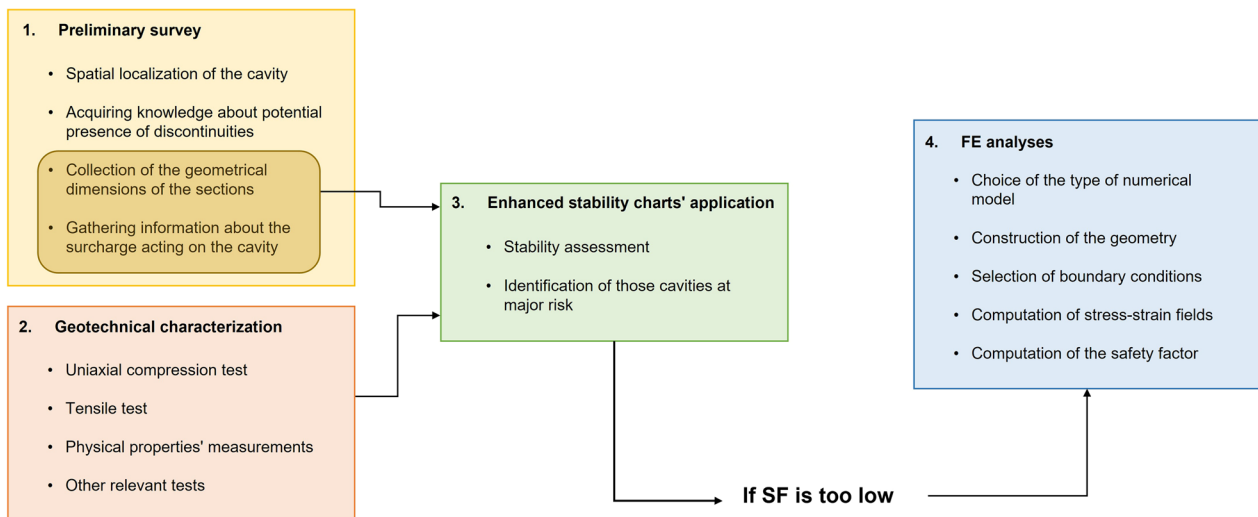

Fig. 17 Methodology scheme

(i.e., the rock mass housing the cavity and other eventual layers overlying the rock stratum). The required physical and mechanical parameters can be gathered by directly performing laboratory investigations or by consulting technical reports and scientific publications. Specifically, uniaxial compressive and tensile tests are typically performed to mechanically characterize the

rock stratum. All the relevant information collected in the previous steps is then used to quantitatively assess the stability of the studied cavities through the enhanced stability chart application. Firstly, the choice of the enhanced stability chart to be used depends on the value of the HB parameter m_i, which is calculated as the ratio between the uniaxial compressive
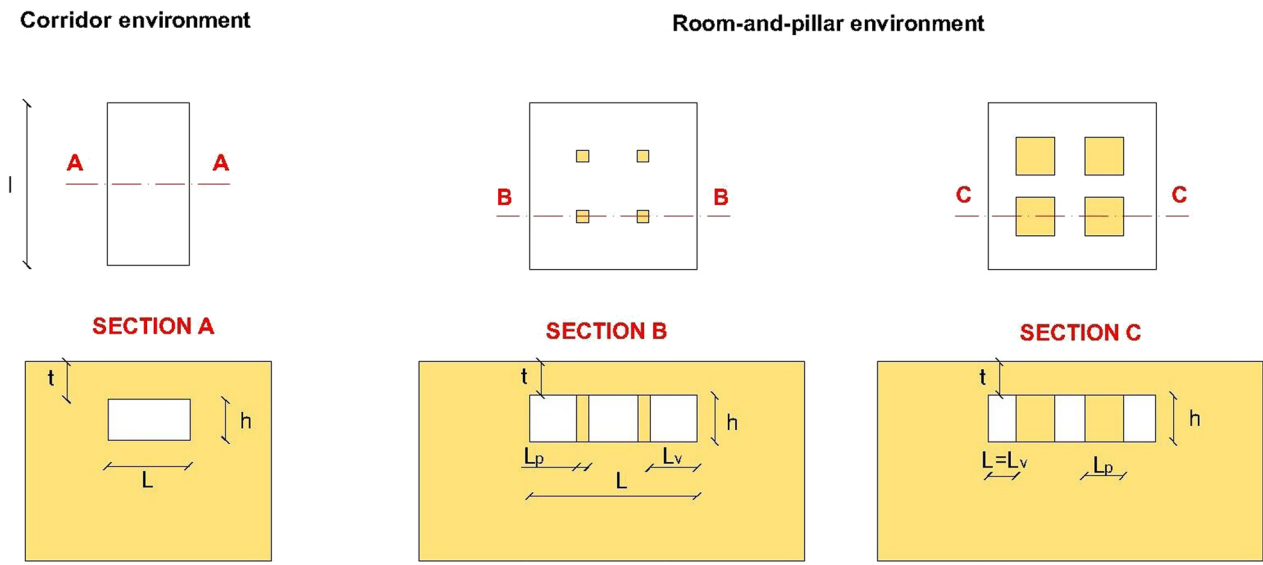
Corridor environment   **Room-and-pillar environment**

Fig. 18 Geometrical parameter choice for different underground cave environments, where: L_p is the thickness of the pillar, L_v is the void width, L is the width of the chosen section, h is its height and t is the roof thickness

and tensile strengths (Cai 2010). Subsequently, the width and the height of the underground cavity section identify the value of the shape factor, L/h, which is related to a specific sub-category of the stability chart. Each identified section corresponds to a point on the stability chart. The abscissa of this point is computed as the ratio between the width and the roof thickness, L/t, whereas the ordinate is the ratio between the ultimate value of the uniaxial compressive strength and the vertical stress at the section depth, σ_{cmin}/σ_v. Normally, laboratory uniaxial compression tests are performed on at least three rock specimens, and the resulting value of the uniaxial compressive strength corresponds to the average of the different results. The application of the enhanced stability charts requires the minimum value to compute the point ordinate. The equation to compute the vertical stress at the section depth is the following:

$$\sigma_v = \gamma t + \Delta \sigma_v \qquad (7)$$

where γ is the unit weight of the rock mass and $\Delta \sigma_v$ is the vertical component of an eventual surcharge acting on the load-bearing rock roof (e.g., other soil/rock layers and/or existing buildings). This latter comprises the mechanical contribution coming from other layers of geo-materials above the rock stratum as well as buildings at ground level. Finally, a set of points populates the enhanced stability charts, indicating not only the state of the section (i.e., stable, or unstable), but also an estimate of the safety factor value for every studied section.

According to the proposed methodology, the points in the orange region (i.e., in a range of $1 < SF < 2$) of the enhanced stability charts, are considered at risk, thus requiring more in-depth analyses.

The final step focuses on more advanced and specific analyses regarding those cases that resulted at risk through the application of proper FE models, which can provide additional insights into the potential failure mechanism, mobilized stresses and strains, and the associated SF value.

Discussion

The present work provides a comprehensive methodology for assessing the stability of soft rock underground environments in preliminary large-scale investigations as well as an advancement of the mechanically-based stability charts, previously developed by Perrotti et al. (2018), which represent the third step of the aforementioned methodology. Figure 19 highlights the advantage of using enhanced stability charts over those proposed by Perrotti et al. (2018) through the application of a simple illustrative case. On both graphs, there are two representative points characterized by the same vertical distance from the failure envelope. Using Perrotti et al. stability charts, it is challenging to determine which of the two sections is at greater risk. From a practical point of view, the user would conduct more in-depth analyses of both cases in the absence of additional information (i.e., SF). Conversely, the enhanced stability chart is capable
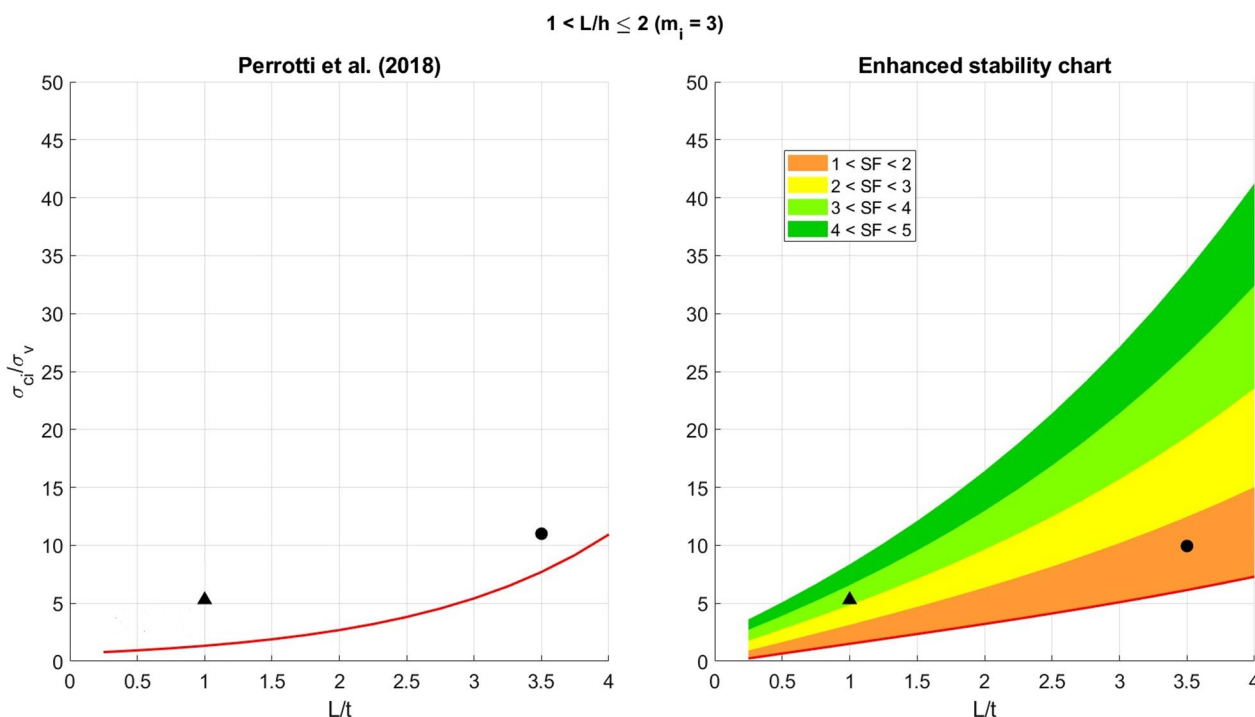
Fig. 19 Comparison between the application of the FEM-based stability charts developed by Perrotti et al. (2018) and the advanced version provided in this work

of straightforwardly identifying the circle as the most prone-to-instability case, overcoming the uncertainties associated with simpler tools.

The advanced stability charts inherit the reliability features of their previous version in terms of validating collapse phenomena, as demonstrated in the Marsala case study. Perrotti et al. (2019) validated the Marsala failure event by means of FEM-based stability charts developed from a series of 2D parametric numerical analyses with an elastic-perfectly plastic model and a HB failure envelope to simulate rock behavior. The fact that the same outcome is here achieved with the use of equivalent MC-based advanced stability charts corroborates the enhanced tool reliability.

The employment of enhanced stability charts is, however, limited to their applicability hypotheses: rectangular cavity sections, intact rock mass (GSI = 100), disturbance factor, D = 0, and plane-strain configuration. For this reason, the choice of the cavities and sections should be based upon these conditions. The methodology application to the three case studies highlights the reliability of the advanced stability charts when assessing the stability of real sections characterized by rectangular geometries. In fact, only 2 of the 49 analyzed rectangular sections show that the calculated SF values do not belong to the

SF ranges into which the representative points fall (M_ANT_18 and CP_Cav74). However, for these sections, as calculated from specific numerical FE analyses, the value of safety factor is equal, respectively, to 4.05 and 4.23, so resulting greater than the expected range ($3 < SF < 4$) obtained applying enhanced stability charts.

Furthermore, the Canosa di Puglia case study points out the need to investigate the stability of sections with a shape other than rectangular. Also in these specific cases, the enhanced stability chart application suggests a condition in favor of safety. However, future studies need to be addressed to include different section geometries as well as the variability of GSI and D.

The robustness of this advanced tool is accompanied by its simplicity of use. In fact, it requires basic information about the geometrical features of the cavity sections, and the geomechanical parameters can be easily acquired through ordinary laboratory tests performed in the common practice of rock mechanics (i.e., uniaxial compression and indirect tensile tests). Finally, since improved stability charts operate with normalized quantities, they can be used to assess the stability of case studies in other regions of the world that are similar to those of Southern Italy.

Concluding remarks

Cave failure quantitative susceptibility analyses at large scale, such as those carried out at urban scale, can be important in order to develop correct land management policies or to establish a scale of priority for detailed analyses and interventions for caves with high risk of collapse. At present, the available techniques to achieve this goal can be classified as either empirically-based methodologies, which cannot be truly considered quantitative and rigorous due to their large degree of uncertainty, or very sophisticated and detailed numerical models, which require significant computational efforts and data availability. In this regard, the enhanced stability charts, along with the methodology here proposed, provide a useful tool that attempts to meet both requirements: the need for quantitative analysis and the simplicity of a methodology that can be applied to a large number of underground cavities in a straightforward manner. In fact, they require data sets that can be easily gathered through in-situ surveys and standard geotechnical tests, as described in the first two steps of the proposed methodology. For this reason, the approach is believed to save time and economical investments that would be otherwise relevant when dealing with large-scale preliminary stability investigations.

The quantitative estimate of the stability degree provided by the indication of SF range reduces the uncertainty associated with the use of the stability charts proposed by Perrotti et al. (2018), for which the information on stability can only be related to the position of the cave point above the failure envelope. Moreover, the application to the three case studies yielded satisfactory results and corroborated the method reliability, thus allowing to identify those cavities at high risk (i.e., belonging to the SF ranging between 1 and 2), for which more specific and comprehensive investigations (i.e., 3D FE modeling) can be addressed along with appropriate solutions for improving the stability conditions. The great potentials of the enhanced stability charts, corroborated by a good validation, make them an innovative, Straightforward, User-friendly and Mechanically based Method (iSUMM) to be used in preliminary stability assessment analyses.

Appendix

The following table lists the equation describing the SF curves on the enhanced stability charts for each value of the HB parameter m_i, and for every sub-category of the shape factor, L/h (Table 8).

Table 8 Equations of the SF curves for each parameter m_i and shape factor sub-category

	L/h ≤ 1	1 < L/h ≤ 2	2 < L/h ≤ 3	L/h > 3
$m_i = 3$				
SF = 1	$0.018x^3 + 0.0065x^2 + 1.42x + 0.51$	$0.026x^3 - 0.068x^2 + 1.74x - 0.2$	$0.015x^3 + 0.033x^2 + 1.63x - 0.26$	$0.031x^3 - 0.11x^2 + 2.018x - 0.44$
SF = 2	$0.04x^3 + 0.18x^2 + 2.2x + 0.84$	$0.061x^3 - 0.056x^2 + 2.95x + 0.18$	$0.06x^3 - 0.033x^2 + 2.92x + 0.13$	$0.064x^3 - 0.077x^2 + 3.06x + 0.027$
SF = 3	$0.064x^3 + 0.36x^2 + 3x + 1.75$	$0.084x^3 + 0.13x^2 + 3.82x + 0.8$	$0.083x^3 + 0.14x^2 + 3.85x + 0.65$	$0.088x^3 + 0.085x^2 + 4.036x + 0.48$
SF = 4	$0.085x^3 + 0.6x^2 + 3.7x + 2.81$	$0.1x^3 + 0.4x^2 + 4.51x + 1.55$	$0.11x^3 + 0.28x^2 + 4.93x + 1.11$	$0.11x^3 + 0.23x^2 + 5.12x + 0.9$
SF = 5	$0.11x^3 + 0.81x^2 + 4.44x + 3.88$	$0.13x^3 + 0.57x^2 + 5.47x + 2.2$	$0.13x^3 + 0.47x^2 + 5.92x + 1.64$	$0.15x^3 + 0.29x^2 + 6.47x + 1.21$
$m_i = 8$				
SF = 1	$-0.019x^3 + 0.49x^2 + 0.66x + 1.13$	$-0.013x^3 + 0.4x^2 + 1.25x + 0.336$	$-0.03x^3 + 0.534x^2 + 1.17x + 0.29$	$-0.0007x^3 + 0.222x^2 + 2.12x - 0.416$
SF = 2	$0.065x^3 + 0.09x^2 + 3.66x + 0.31$	$0.064x^3 + 0.082x^2 + 3.82x - 0.072$	$0.062x^3 + 0.082x^2 + 3.9x - 0.17$	$0.071x^3 - 0.0084x^2 + 4.116x - 0.3$
SF = 3	$0.11x^3 + 0.36x^2 + 4.73x + 1.5$	$0.11x^3 + 0.3x^2 + 5.24x + 0.66$	$0.11x^3 + 0.25x^2 + 5.43x + 0.44$	$0.12x^3 + 0.18x^2 + 5.63x + 0.27$
SF = 4	$0.14x^3 + 0.81x^2 + 5.57x + 2.9$	$0.14x^3 + 0.74x^2 + 6.32x + 1.57$	$0.14x^3 + 0.73x^2 + 6.56x + 1.14$	$0.14x^3 + 0.68x^2 + 6.81x + 0.84$
SF = 5	$0.17x^3 + 1.25x^2 + 6.54x + 4.42$	$0.17x^3 + 1.17x^2 + 7.435x + 2.55$	$0.18x^3 + 1.09x^2 + 7.9x + 1.92$	$0.18x^3 + 1.04x^2 + 8.18x + 1.54$
$m_i = 16$				
SF = 1	$0.03x^3 + 0.063x^2 + 2.31x + 0.82$	$-0.055x^3 + 0.96x^2 + 0.41x + 0.81$	$-0.066x^3 + x^2 + 0.76x + 0.37$	$-0.0009x^3 + 0.3x^2 + 2.78x - 0.74$
SF = 2	$0.072x^3 + 0.16x^2 + 4.61x - 0.26$	$0.067x^3 + 0.24x^2 + 4.46x - 0.52$	$0.028x^3 + 0.58x^2 + 3.7x - 0.12$	$0.077x^3 + 0.105x^2 + 4.9x - 0.75$
SF = 3	$0.1x^3 + 0.74x^2 + 5.78x + 1.32$	$0.11x^3 + 0.65x^2 + 6.33x + 0.3$	$0.1x^3 + 0.68x^2 + 6.4x + 0.15$	$0.11x^3 + 0.53x^2 + 6.86x - 0.18$
SF = 4	$0.16x^3 + 1.15x^2 + 7.58x + 2.7$	$0.18x^3 + 0.87x^2 + 8.86x + 0.9$	$0.18x^3 + 0.84x^2 + 9.17x + 0.44$	$0.19x^3 + 0.76x^2 + 9.46x + 0.15$
SF = 5	$0.22x^3 + 1.67x^2 + 9.16x + 4.36$	$0.24x^3 + 1.36x^2 + 10.74x + 1.92$	$0.24x^3 + 1.25x^2 + 11.37x + 1.15$	$0.25x^3 + 1.14x^2 + 11.73x + 0.74$

Author contributions

FAM: Methodology, software, validation, formal analysis, investigation, data curation, writing—original draft; NLF: Conceptualization, supervision, methodology, writing—original draft; MP: Methodology, supervision, writing—original draft; PL: Conceptualization, supervision, project administration, funding acquisition, writing-review and editing methodology.

Declarations

Competing interests

The authors declare no competing interests.

References

Andriani GF, Walsh N (2010) Petrophysical and mechanical properties of soft and porous building rocks used in Apulian monuments (south Italy). Geol Soc Lond Spec Publ 333(1):129–141

Aydan O, Tano H, Sakamoto A, et al (2005) A real-time monitoring system for the assessment of stability and performance of in abandoned room and pillar lignite mines. In: PostMining 2005, November 16–17, Nancy, France

Bonamini M, Di Maggio C, Lollino P et al (2013) Sprofondamenti di origine antropica nell'area di marsala (sicilia occidentale) analizzati mediante rilievi in sito e analisi numerica dei processi di instabilità nelle cave sotterranee. Mem Descr Carta Geol d'It 93:105–120 (**in Italian**)

Cai M (2010) Practical estimates of tensile strength and Hoek–Brown strength parameter m_i of brittle rocks. Rock Mech Rock Eng 43(2):167–184

Carter T (2014) Guidelines for use of the scaled span method for surface crown pillar stability assessment. In: Ontario ministry of northern development and mines, Ontario, pp 1–34

Castellanza R, Lollino P, Ciantia M (2018) A methodological approach to assess the hazard of underground cavities subjected to environmental weathering. Tunn Undergr Space Technol 82:278–292

Ciantia MO, Castellanza R, Di Prisco C (2015) Experimental study on the water-induced weakening of calcarenites. Rock Mech Rock Eng 48(2):441–461

Contrucci I, Klein E, Cao NT et al (2011) Multi-parameter monitoring of a solution mining cavern collapse: first insight of precursors. CR Geosci 343(1):1–10

Coviello A, Lagioia R, Nova R (2005) On the measurement of the tensile strength of soft rocks. Rock Mech Rock Eng 38(4):251–273

Drumm EC, Aktürk Ö, Akgün H et al (2009) Stability charts for the collapse of residual soil in karst. J Geotech Geoenviron Eng 135(7):925–931

Evangelista A, Pellegrino A, Viggiani C (1991) Cavità e gallerie nel tufo giallo napoletano. In: Atti IX Ciclo Conf. MIR, Le opera in sotterraneo e il rapporto con l'ambiente, Patron Editore, Falla Castelfranchi M (**in Italian**)

Fazio NL, Perrotti M, Lollino P et al (2017) A three-dimensional back-analysis of the collapse of an underground cavity in soft rocks. Eng Geol 228:301–311

Federico F, Screpanti S (2003) Effects of filling shallow room and pillar mines in weak pyroclastic rock. In: Geotechnical problems with man-made and man influenced grounds, Prague, Czech Republic, 25–28th August 2003, pp 673–678

Ferrero AM, Segalini A, Giani GP (2010) Stability analysis of historic underground quarries. Comput Geotech 37(4):476–486

Fiore A, Parise M (2013) Cronologia degli eventi di sprofondamento in puglia, con particolare riferimento alle interazioni con l'ambiente antropizzato. Memorie Descrittive della Carta Geologica d'Italia 93:239–252 (**in Italian**)

Fiore A, Fazio N, Lollino P et al (2018) Evaluating the susceptibility to anthropogenic sinkholes in Apulian calcarenites, southern Italy. Geol Soc Lond Spec Publ 466(1):381–396

Fraldi M, Guarracino F (2009) Limit analysis of collapse mechanisms in cavities and tunnels according to the Hoek–Brown failure criterion. Int J Rock Mech Min Sci 46(4):665–673

Gesualdo A, Minutolo V, Nunziante L (2001) Failure in Mohr Coulomb soil cavities. Can Geotech J 38(6):1314–1320

Goh ATC, Zhang W (2012) Reliability assessment of stability of underground rock caverns. Int J Rock Mech Min Sci 55:157–163

Goodings DJ, Abdulla WA (2002) Stability charts for predicting sinkholes in weakly cemented sand over karst limestone. Eng Geol 65(2–3):179–184

Guenzi D, Godone D, Allasia P et al (2022) Brief communication: monitoring a soft-rock coastal cliff using webcams and strain sensors. Nat Hazard 22(1):207–212

Hoek E, Brown ET (1997) Practical estimates of rock mass strength. Int J Rock Mech Min Sci 34(8):1165–1186

Hoek E, Martin C (2014) Fracture initiation and propagation in intact rock-a review. J Rock Mech Geotech Eng 6(4):287–300

Hoek E, Carranza-Torres C, Corkum B et al (2002) Hoek–Brown failure criterion-2002 edition. Proc NARMS-Tac 1(1):267–273

Keawsawasvong S, Shiau J (2022) Stability of spherical cavity in Hoek–Brown rock mass. In: Rock mechanics and rock engineering, pp 1–12

Lollino P, Martimucci V, Parise M (2013) Geological survey and numerical modeling of the potential failure mechanisms of underground caves. Geosyst Eng 16(1):100–112

Lollino P, Pagliarulo R, Trizzino R et al (2021) Multi-scale approach to analyse the evolution of soft rock coastal cliffs and role of controlling factors: a case study in south-eastern Italy. Geomat Nat Haz Risk 12(1):1058–1081

Mancini F, Castagnetti C, Rossi P et al (2017) An integrated procedure to assess the stability of coastal rocky cliffs: From UAV close-range photogrammetry to geomechanical finite element modeling. Remote Sens 9(12):1235

Mastropasqua F, Laghezza E (2009) Progetto per la realizzazione di un parco eolico nel comune di canosa di puglia (bat). Technical Report (**in Italian**)

Matsui T, San KC (1992) Finite element slope stability analysis by shear strength reduction technique. Soils Found 32(1):59–70

Nisio S (2009) I sinkholes nelle aree di pianura italiane: i risultati del "progetto sinkhole". Atti 2nd Workshop internazionale: I sinkholes Gli sprofondamenti catastrofici nell'ambiente naturale ed in quello antropizzato (**in Italian**)

Nisio S (2017) Aree soggette ai sinkholes. ISPRA Annuario dei dati Ambientali (**in Italian**)

Nisio S (2018) I sinkholes antropogenici nelle cittià taliane. Qualità dell'ambiente urbano - XIV Rapporto (2018) ISPRA Stato dell'Ambiente (**in Italian**)

Parise M (2010) The impacts of quarrying in the Apulian karst (Italy). In: Advances in research in karst media. Springer, pp 441–447

Parise M (2012) A present risk from past activities: sinkhole occurrence above underground quarries. Carbonates Evaporites 27(2):109–118

Parise M, Lollino P (2011) A preliminary analysis of failure mechanisms in karst and man-made underground caves in southern Italy. Geomorphology 134(1–2):132–143

Parise M, Vennari C (2017) Distribution and features of natural and anthropogenic sinkholes in Apulia. In: EuroKarst 2016, Neuchâtel. Springer, pp 27–34

Pellicani R, Spilotro G, Gutiérrez F (2017) Susceptibility mapping of instability related to shallow mining cavities in a built-up environment. Eng Geol 217:81–88

Perrotti M, Lollino P, Fazio N et al (2018) Finite element-based stability charts for underground cavities in soft calcarenites. Int J Geomech 18(7):04018071

Perrotti M, Lollino P, Fazio NL et al (2019) Stability charts based on the finite element method for underground cavities in soft carbonate rocks: validation through case-study applications. Nat Hazard 19(10):2079–2095

Plaxis 2D (2020) Reference manual. In: CONNECT Edition V2003, Bentley

Suchowerska AM, Merifield RS, Carter JP et al (2012) Prediction of underground cavity roof collapse using the Hoek–Brown failure criterion. Comput Geotech 44:93–103

Vattano M, Parise M, Lollino P, et al (2013) Examples of anthropogenic sinkholes in Sicily and comparison with similar phenomena in southern Italy. In: 13th Multidisciplinary conference on sinkholes and the engineering and environmental impacts of karst

Zhang R, Chen G, Zou J et al (2019) Study on roof collapse of deep circular cavities in jointed rock masses using adaptive finite element limit analysis. Comput Geotech 111:42–55

Zimbardo M (2009) Comportamento meccanico di rocce tenere: le calcareniti di palermo e marsala. PhD Thesis (**in Italian**)

Publisher's Note